

# Fully Developed Turbulent Flow in a Curved Rectangular Duct\*

Yoshinori KITA\*\*, Makoto OKAZAKI\*\*\*,  
Kōji HIROSE\*\* and Satoshi TANAKA\*\*\*\*

Fully developed flows in a curved rectangular duct having a breadth/curvature-radius ratio of 0.25 are studied experimentally. A flow-turning angle of more than  $150^\circ$  is required for the flow to reach a fully developed state in any duct which has an aspect ratio (height/breadth) of the cross section ranging from 0.4 to 16. In the case of low aspect ratios, the main flow has a forced vortex-type velocity distribution, and has a free vortex-type distribution at high aspect ratios. Concerning the skewed boundary layer on the end plate, similarity exists in the secondary flow velocity distributions. It was found that the profile of the distribution is the same as one of two-dimensional wall jets, and that the thickness of the secondary flow boundary layer should be considered separately from that of the main flow.

**Key Words:** Curved Duct, Rectangular Cross Section, Boundary Layer, Secondary Flow, Turbulent Flow, Reynolds Shear Stress

## 1. Introduction

Flows in fluid machinery are mostly three-dimensional and turbulent. The nature of the flows in three-dimensional turbulent boundary layers which grow on the passage walls of the fluid machinery is very complex, and the respective kinds of flow patterns are numerous. To understand the characteristics of such flows in three-dimensional boundary layers, it is necessary to measure accurately the velocity components of the main flow and the secondary flow as well, and to closely examine these measurements.

Since, in most flows, the magnitude of the velocity component of the secondary flow is one order smaller than that of the main flow, it is very difficult to

measure accurately such a small velocity component. Therefore, the first step of studying such complex flows might be to measure equilibrium skewed boundary layers having strong secondary flow components, as Senoo suggested<sup>(1)</sup>. To obtain such boundary layer, a curved rectangular duct having a small aspect ratio of 0.4 and a duct turning angle of  $270^\circ$  is used in this work.

In the first half of this paper, the flow development along the duct and boundary layers on both concave and convex walls of the duct in the fully developed flow region are discussed, and compared with the results obtained by other researchers<sup>(2)-(5)</sup> in ducts having large aspect ratios but having almost the same breadth/curvature-radius ratio as ours.

In the second half of this paper, an equilibrium skewed turbulent boundary layer grown up on the end plate of the duct is studied. In particular, the similarity in velocity distributions of the secondary flow component, the relation between two characteristic lengths: one is for the main flow boundary layer and the other for the secondary flow, and the distributions of flow skewed angle and of Reynolds shear stress are investigated.

\* Received 15th April, 1987. Paper No. 85-0187A, 0188A

\*\* Department of Mechanical Engineering, Okayama University, 3-1-1 Tsushima-Naka, Okayama, 700, Japan

\*\*\* Mitsubishi Electric Corporation, 8-1-1 Tsukaguchi-Honmachi, Amagasaki, 661, Japan

\*\*\*\* Kawasaki Heavy Industries, Ltd., 1 Kawasaki-cho, Sagami-hara, 504, Japan

## 2. Experimental Apparatus and Methods

The curved duct, used here and shown in Fig. 1, has a rectangular cross section of the following dimensions: the breadth ( $2B$ ) is 200 mm and the height ( $2H$ ) is 80 mm, so that the hydraulic diameter ( $D$ ) is about 114 mm. The duct axis has a curvature radius ( $R$ ) of 800 mm and a turning angle of 270 degrees. Figure 1 also shows the coordinate system adopted here: the  $x$ -axis, which is parallel to the duct centerline, is attached onto the lower end plate and is scaled with  $R \cdot \phi$ , where  $\phi$  is the duct turning angle, radius  $r$  is as it stands, and  $z$  is perpendicular to the  $x$ - $r$  plane and directed vertically upwards. The corresponding three velocity components are denoted by  $U_\phi$ ,  $U_r$ , and  $U_z$ , respectively.

Figure 2 shows the experimental apparatus used. It consists of bellmouth, mesh, and 2-meter-long upstream tangent, through which the flow is lead to the curved duct inlet, and the duct is followed by a 2-meter-long downstream tangent. The flow is then lead to the suction side of the blower, through a 5-meter-long straight tangent and a surge chamber. These tangents have the same cross sectional configuration that the curved duct has.

Four wall-pressure taps are located in the same cross section: one on both the upper and lower end

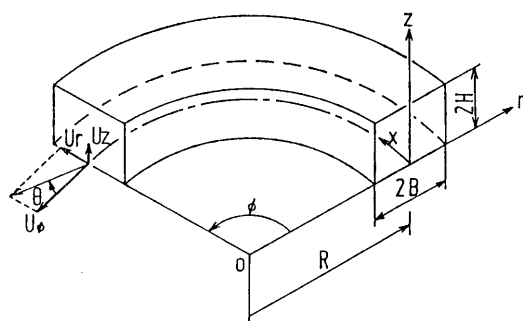


Fig. 1 Coordinate system

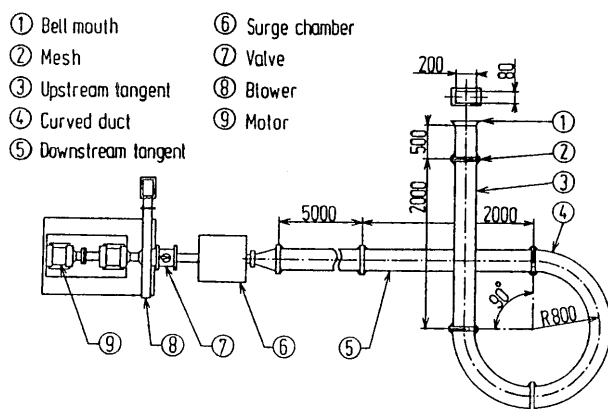


Fig. 2 Apparatus

plates at  $r=R$ , and one on each side wall at  $z=H$ . The cross sections having these pressure taps are distributed along the duct in the following manner: at every 0.1 meters within the upstream tangent, at every 15 degrees of the duct turning angle along the duct, and at every 0.2 meters within the downstream tangent.

The flow in the fully developed flow region is measured by a 5-hole pitot tube and an  $X$ -type hot-wire anemometer: in the cross section at the  $\phi=195^\circ$  station, these probes are traversed in the  $z$ -direction at  $(r-R)/B=0, \pm 0.5$ , and  $\pm 0.9$ , respectively, and traverses in the  $r$ -direction are also made at three nondimensional heights of  $z/H=1.0, 0.5$ , and  $0.25$ .

A preliminary experimental check showed that (1) the flows on the upper and the lower half side of the duct cross section are symmetrical with respect to  $z/H=1.0$ , (2) the flow in the region of  $195^\circ < \phi < 225^\circ$  is a fully developed turbulent flow, and (3) the flow pattern in the duct is not changed in the range of Reynolds number  $Re(=D \cdot U_m/\nu)$  from  $0.93 \times 10^5$  to  $1.36 \times 10^5$ , where  $U_m$  denotes the cross-sectional mean flow velocity.

## 3. Main Flow

In advance of examining the skewed boundary layer on the end plate, the main flow field, which covers most of the cross section, should be mentioned.

### 3.1 Wall static pressure

Figure 3 shows the static pressure distribution along the duct measured on the inner and outer wall surfaces at the height of  $z/H=1.0$ . The ordinate is the nondimensionalized pressure difference between the wall static pressure and the corresponding pressure at the duct axis denoted by  $P_{T,B}$ .

According to the figure, the influence of the curved duct on the axial pressure distribution in tan-

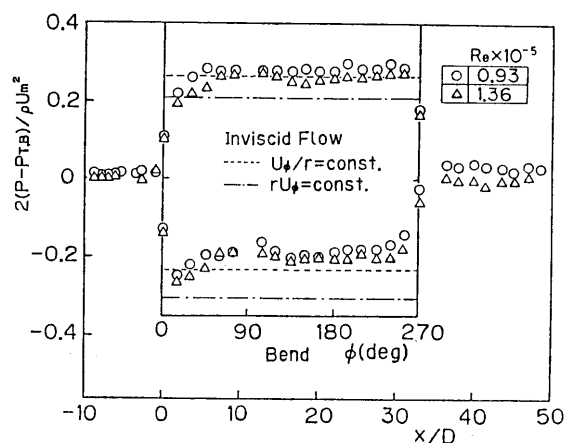


Fig. 3 Static pressure distributions on both side walls along duct

gents exists a few diameters ( $2.5D$ ) both upstream from the duct inlet and downstream from the duct outlet. The influence of the change in the duct curvature from straight to curved, or vice versa, on the flow in the curved duct reaches the  $\phi=90^\circ$  station in the duct entry region and the  $45^\circ$  upstream station from the duct outlet in the duct exit region.

Thus, the region where the wall static pressure decreases linearly along the duct is restricted to the region of  $90^\circ < \phi < 225^\circ$ , where the pipe friction factor for the curved duct is about 20~30 per cent larger than that for the straight duct having the same cross section.

The dotted and chained lines in Fig. 3 indicate the predicted pressure distributions for two-dimensional forced and free vortex-type whirl flows, respectively. Comparing the measurements with the predictions, the measured pressure distribution on the outer wall shows a better agreement with the prediction by a forced vortex-type flow than with the one by a free vortex-type flow. On the inner wall surface, however, the measured pressure seems firstly to reach that of a free vortex-type flow, but in the region of  $\phi > 90^\circ$ , the pressure increases to a predicted value by a forced vortex-type flow which is similar to that on the outer wall.

### 3.2 The required duct turning angle for flow to develop

Axial pressure gradient, friction coefficient  $C_f$ , and the angle  $\theta_w$  of the limiting streamline on the end plate measured from the  $x$ -direction have almost constant values along the duct in the region of  $150^\circ < \phi < 225^\circ$ , though it is not shown in this paper. It tells us that, there, the duct flow is a fully developed flow state.

In the ducts having large aspect ratio, a fully developed flow was obtained in the region of  $150^\circ < \phi < 210^\circ$  in Wattendorf's apparatus<sup>(2)</sup> and in the region of  $172^\circ < \phi < 236^\circ$  in Eskinazi's rig<sup>(3)</sup>.

As a result, it might be said that when the value of  $B/R$  of a duct is about 0.13, a duct turning angle of  $150^\circ$  or more is required for the flow to become fully developed, regardless of the duct aspect ratio.

### 3.3 Flow distribution in the duct breadth

Figure 4 shows velocity and Reynolds shear stress distributions in the duct breadth at  $z/H=1.0$  in a fully developed flow region. Nondimensionalized  $rU_\phi$  is not constant over the breadth, but increases with the radius.  $U_\phi/r$  remains almost constant over the breadth, at a value equal to  $U_m/R$ . On the contrary, according to the experimental results by Wattendorf<sup>(2)</sup> and Ellis and Joubert<sup>(4)</sup>, the main flow in the fully developed flow region of a curved duct is of a free-vortex type.

A comparison between these results may indicate that the fully developed flow in a curved duct having the  $B/R$  ratio of about 0.13 is of the free-vortex type in the wide area of the duct cross section when the aspect ratio  $H/B$  is larger than two<sup>(5)</sup>, but is of the forced-vortex type due to the very strong induced secondary flow in the case where the aspect ratio  $H/B$  is smaller than two.

The cross flow rate  $rU_r/RU_m$  has an almost constant value of 0.03~0.04. The magnitude may be calculated as follows: on the assumption that in the momentum equation in the  $\phi$ -direction, the  $U_z$  term and shear stress terms can be neglected, and that  $U_\phi/r$  is equal to  $U_m/R$ , the momentum equation is reduced to the following equation:

$$\frac{rU_r}{RU_m} = -\frac{1}{4} \frac{d}{d\phi} \left( \frac{P}{\rho U_m^2 / 2} \right).$$

In our experiment, the nondimensionalized axial pressure gradient involved in this equation was about  $-0.16$ . The value of  $rU_r/RU_m$  then becomes 0.04 and shows good agreement with the experimental value seen in Fig. 4. In this way, we concluded that the equation could be used to predict the magnitude of  $U_r$  from  $dP/rd\phi$ .

Measurements of the Reynolds shear stress,  $-\rho \overline{u_r u_\phi}$ , shown in Fig. 4 were almost equal to zero over a wide area of the duct cross section, except near the side wall. The mark  $\diamond$  on the ordinate axis shows the wall shear stress,  $\tau_w$ , which was evaluated using the Clauser chart. The evaluated values show good agreement with the values extrapolated from the measured  $-\rho \overline{u_r u_\phi}$  values.

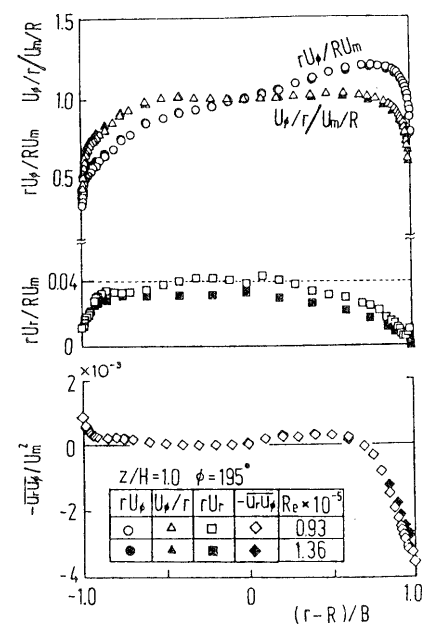


Fig. 4 Flow distributions in breadth

In Fig. 5, the secondary flow pattern in the same cross section is shown by velocity vectors. Near the end wall, a strong inward flow is observed over the duct width, and the center of a flatly depressed vortex is located at  $z/H=0.25$ .

### 3.4 Boundary layers on both side walls

Figure 6 shows the distributions of three kinds of boundary layers on the inner and outer wall surfaces, which are defined and evaluated from the profiles of  $U_\phi$ ,  $U_\phi/r$ , and  $rU_\phi$ , and are denoted by  $\delta_{U_\phi}$ ,  $\delta_{U_\phi/r}$ , and  $\delta_{rU_\phi}$ , respectively. Figure 6 also shows the thickness  $\delta_{\log}$ , over which the velocity distribution starts to deviate from the wall law, and the position at which Reynolds shear stress  $-\rho \overline{u'v'}$  becomes zero.

The first three boundary layer thicknesses on the inner and outer wall surfaces are almost constant in the  $z$ -direction, unlike the distribution of nearby secondary flow streamlines.  $\delta_{\log}$  is also almost constant along the  $z$ -direction. The ratio of  $\delta_{\log}$  to any one of the three kinds of  $\delta$  ranges from 0.15 to 0.25, which are ordinal values for ordinal turbulent boundary layers on a flat plate.

On the outer wall surface or concave wall, Reynolds shear stress  $-\rho \overline{u'v'}$  becomes zero not at the edge of the boundary layer, but outside the boundary layer as in a two-dimensional wall jet flow. On the

inner wall surface, however, Reynolds shear stress falls to zero at  $0.4\delta$  inside the boundary layer, except at measurements at  $z/H=1.0$ . This trend of Reynolds shear stress distribution in the boundary layer on convex walls can be seen in the measurements by So<sup>(6)</sup> and Gillis<sup>(7)</sup>.

## 4. Measurements of the Equilibrium Boundary Layer on the End Plate

### 4.1 Boundary layer thickness

Some characteristic lengths for the boundary layer on the end plate at  $\phi=195^\circ$  are shown in Fig. 7, where  $\delta_{U_r=0}$  is the distance from the wall at which the radial velocity component  $U_r$  falls to zero, and  $\delta_{2.5b}$  is 2.5 times the half-value breadth  $b$  of  $\Delta r U_r$ , which will be defined later as the secondary flow boundary layer thickness and denoted by  $l$ .

According to Fig. 7(a),  $\delta_{\log}$  locates near  $\delta_{U_\phi}$ . This means that  $U_\phi$  follows the log law until  $U_\phi$  almost reaches its maximum value,  $U_{\phi \max}$ , unlike on the side walls shown in Fig. 6.  $\delta_{U_r=0}$  is very close to  $\delta_{U_\phi}$ ;  $\delta_{2.5b}$  is about 2.2 times that of  $\delta_{U_\phi}$ . While the characteristic lengths decrease with radius  $r$ , the length  $\delta_{U_\phi U_z=0}$  increases with radius  $r$ . This trend is similar to the distribution of the friction coefficient  $C_f (=2\tau_w/\rho U_m^2)$ .

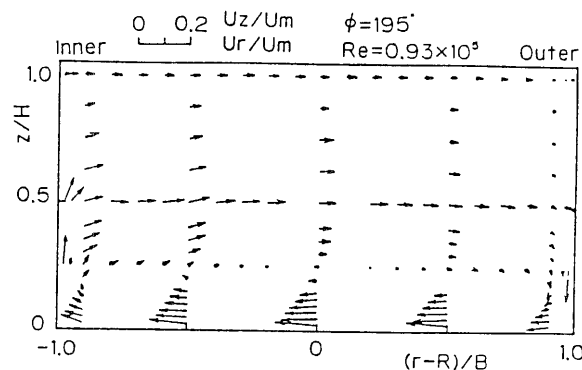


Fig. 5 Secondary flow velocity vector

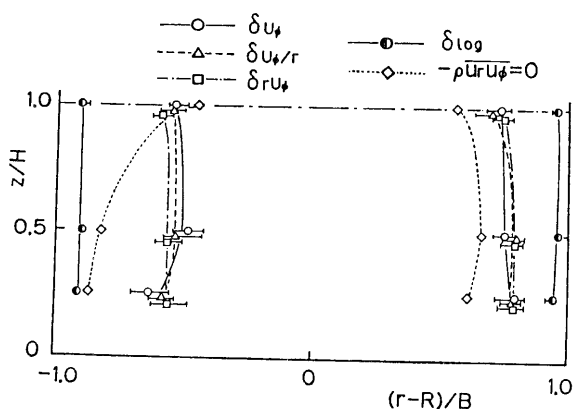
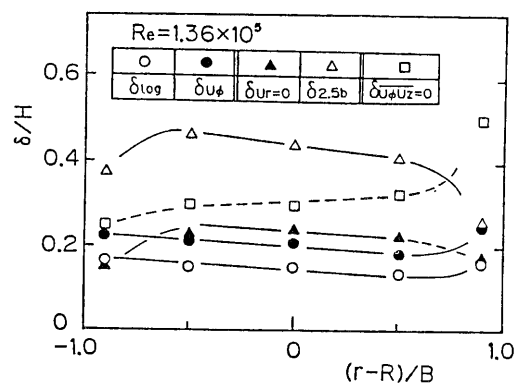
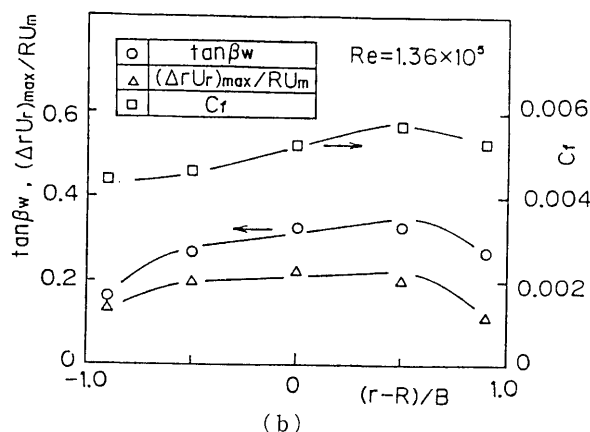


Fig. 6 Boundary layer thickness on both side walls



(a)



(b)

Fig. 7 Boundary layer on the end plate

Figure 7(b) shows  $C_f$  and the following two quantities, which will be defined in section 5.1: the maximum secondary flow velocity  $(\Delta rU_r)_{\max}$  and the tangent of  $\beta_w$ , which is the angle of the limiting streamline measured from the main flow direction but not from the  $\phi$ -direction.

#### 4.2 $rU_\phi$ distribution in the $z$ -direction

Figure 8 shows the  $rU_\phi$  distribution in the  $z$ -direction obtained at five radial positions:  $(r-R)/B = 0, \pm 0.5$ , and  $\pm 0.9$ . The  $rU_\phi$  value increases with the radius of the measured position. In each profile,  $rU_\phi$  exhibits a maximum value at  $z/H = 0.25$ , and decreases slowly thereafter. In the region where  $z/H > 0.5$ ,  $rU_\phi$  remains almost constant.

#### 4.3 Profiles of $rU_r$ and yaw angle, $\theta$ , in the $z$ -direction

The yaw angle  $\theta$  of flow is defined as the angle between the flow streamline and the duct axis, as shown in Fig. 1. The profiles of  $rU_r$  and  $\theta$  in the  $z$ -direction are shown in Figs. 9 and 10, respectively, and these are complement to Fig. 8.

According to Fig. 9,  $rU_r$  has a large negative value near the end wall, which indicates inwards fluid flow. In the region where  $z/H > 0.25$ ,  $rU_r$  is positive and reaches a maximum value near  $z/H = 0.5$ ; there-

after, it decreases slowly. This trend is the same at other different radii, but the measuring positions of  $(r-R)/B = \pm 0.9$  were located in each side wall boundary layer, as was seen in Figs. 5 and 6, and the obtained profiles at these positions are somewhat different from those away from the side walls.

In Fig. 10, the profile of the yaw angle  $\theta$  is very similar to that of  $rU_r$ , and  $\theta$  reaches its maximum value  $\theta_{\max}$  near  $z/H = 0.5$ . In Fig. 10, there is no such region where  $\theta$  remains constant in the  $z$ -direction, as could be found in usual skewed boundary layer flow. The angle  $\theta_w$ , which is the value of  $\theta$  at  $z/H = 0$  and means the limiting streamline direction, is estimated by extrapolating the values of  $\theta$  to the wall.

### 5. Similarity in Velocity Profile

#### 5.1 $U_r$ and half-value breadth $b$

For nondimensional representation of the data, the measured  $rU_r$  were rescaled in such way as shown in Fig. 11, where  $\Delta rU_r = (rU_r)_{\max} - rU_r$ , and  $b$  is defined as the distance from the end wall at which point  $\Delta rU_r$  becomes equal to the half of its maximum value  $(\Delta rU_r)_{\max}$ , that is,  $(rU_r)_{\max} - (rU_r)_{\min}$ . Unfortunately, we could not obtain  $(rU_r)_{\min}$  experimentally. It was estimated by applying Mager's secondary flow

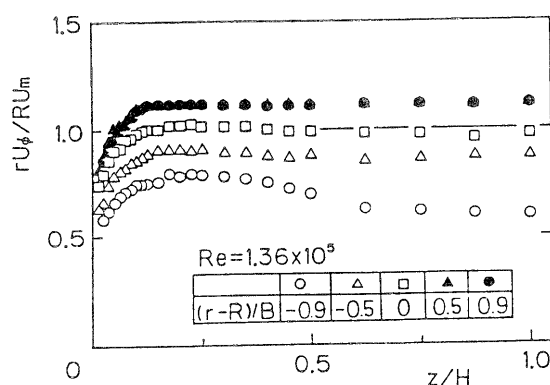


Fig. 8  $rU_\phi$  distribution in  $z$ -direction

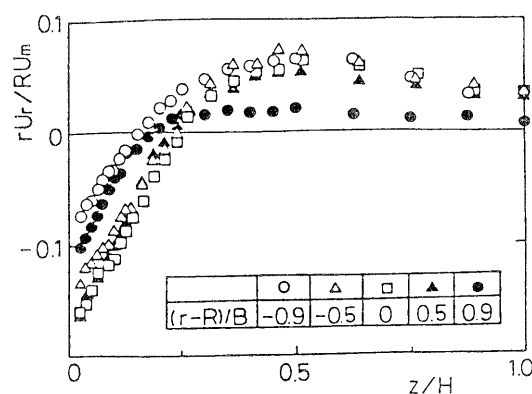


Fig. 9  $rU_r$  distribution in  $z$ -direction

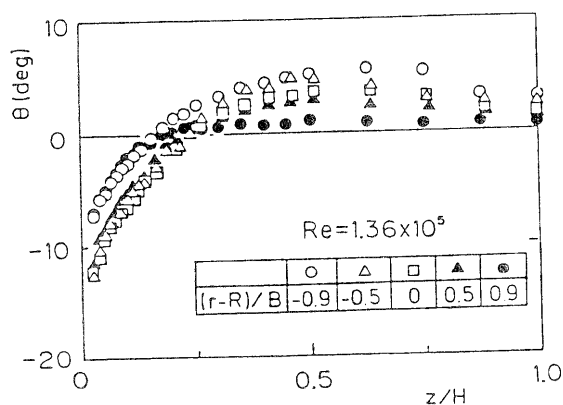


Fig. 10 Flow yaw angle,  $\theta$ , distribution

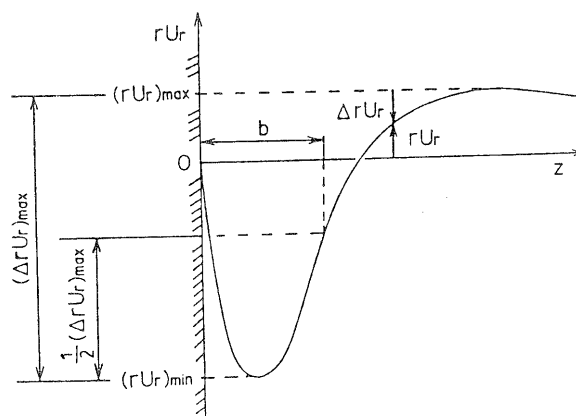


Fig. 11  $rU_r$  and the half-value breadth  $b$

model only to the flow very close to the end wall as stated in the appendix.

Using  $(\Delta r U_r)_{\max}$  and  $b$ , Fig. 9 was replotted in Fig. 12. In Fig. 12, the profiles at  $(r-R)/B = \pm 0.9$  in the side wall boundary layer and those obtained away from the boundary layer collapse onto each other.

The value of  $\Delta r U_r / (\Delta r U_r)_{\max}$  reaches unity immediately at a short distance from the wall. From this point until large  $z/b$ , measurements coincide with the solid line which shows the velocity profile of wall jets given by Verhoff<sup>(8)</sup>, and also with the broken line which shows a simple approximation for the region of large  $z/b$ :  $\Delta r U_r / (\Delta r U_r)_{\max} = \exp(-\ln 2 \cdot (z/b)^2)$ . Although the velocity component  $U_r$  in the curved duct is induced by the unbalance between centrifugal forces and forces due to the radial pressure gradient, the profile of  $U_r$  is very similar to that of the two-dimensional wall jet which is produced by the momentum differences.

It is shown in Fig. 12 that  $\Delta r U_r / (\Delta r U_r)_{\max}$  reaches 0.01 at about  $z/b = 2.5$  in any measuring position. Usually, the boundary layer velocity thickness is defined as the distance from the wall at which velocity is one per cent lesser than the main flow velocity. Then, it might be reasonable to define the secondary flow boundary layer thickness  $l$  with the above mentioned  $2.5b$ .

In Fig. 10, there is no region where the flow angle  $\theta$  remains constant; hence, let us use  $\theta_{\max}$  as a reference point and rescale  $\theta$  in the same way as was done for  $r U_r$  in Fig. 11, i. e., the new variable  $\beta$  is defined by  $\theta_{\max} - \theta$  and  $\beta_w$  is  $\theta_{\max} - \theta_w$ , where  $\theta_w$  is an extrapolated value, as mentioned previously.

The ratio  $\tan \beta / \tan \beta_w$  is plotted against  $z/b$  in Fig. 13. Figure 13 shows that measurements have a similar distribution at any measuring position, and that the ratio falls to zero near  $z/b = 2.5$  as  $\Delta r U_r$  did in Fig. 12. The solid line in Fig. 13 shows the following equation, and gives a good approximation for the

measurement.

$$\left. \begin{aligned} g &= \tan \beta / \tan \beta_w = (1 - z/l)^2 \\ l &= 2.5b \end{aligned} \right\} \quad (1)$$

## 5.2 $U_\phi$ distribution against $z/b$

In the previous section, it was found that the half-value breadth  $b$  can be one of the characteristic lengths for  $U_r$  and  $\theta$ . In this section, it will be studied whether  $b$  could also be a characteristic length for  $U_\phi$ .

Figure 14 shows the profiles of  $U_\phi / U_{\phi 2.5b}$  against  $z/b$ , where  $U_{\phi 2.5b}$  means  $U_\phi$  at  $z = 2.5b$ . The three profiles, which were obtained at  $(r-R)/B = 0$  and  $\pm 0.5$  and marked with  $\triangle$ ,  $\square$ , and  $\blacktriangle$ , respectively, coincide with each other. The profiles have the maximum value 1.04 at  $z/b = 1.2$ , and at  $z/b > 2.5$   $U_\phi / U_{\phi 2.5b}$  remains almost constant. The other two measurements at  $(r-R)/B = \pm 0.9$  fall on the same profile as that mentioned above, even though they were obtained in the side wall boundary layer; thus,  $b$  can also be a characteristic length for  $U_\phi$ .

Judging from Figs. 12~14, the secondary flow boundary layer thickness  $l$  can be defined by  $2.5b$  in Eq. (1).

## 5.3 Mainflow boundary layer thickness $\delta$ and secondary flow boundary layer thickness $l$

For the representation of the velocity distribution in turbulent skewed boundary layers, the following Mager's model is well-known and widely used.

$$u/U = G(z/\delta), \quad G(z/\delta) = (z/\delta)^{1/n} \quad (2)$$

$$w/U = \epsilon \cdot G \cdot g, \quad \epsilon = \tan \beta_w \quad (3)$$

where  $U$  is main flow velocity and  $\beta$  is flow angle measured from the main flow direction.

In Mager's model, the proposed secondary flow boundary layer thickness  $l$ , which is included in the  $g$  function in Eq. (3), is set equal to the main flow boundary layer thickness  $\delta$ .

In fully developed duct flow, there is no clear main flow, so that when Mager's model is to be applied to duct flow, a problem arises as to how the main flow should be selected. In this paper, as for the skewed

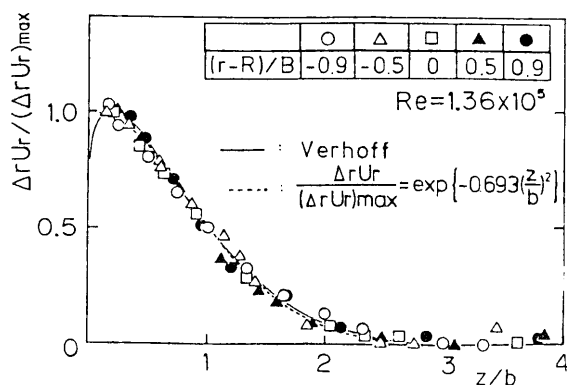


Fig. 12  $\Delta r U_r$  distribution

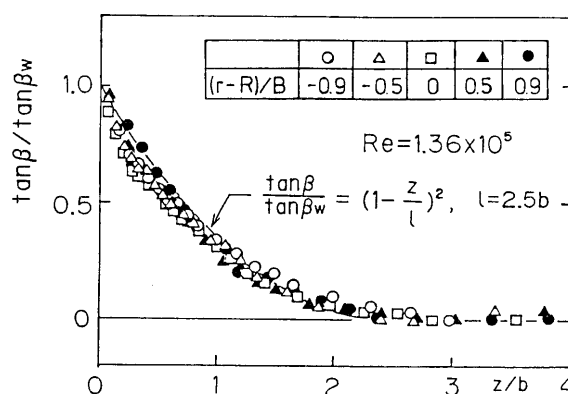


Fig. 13 Flow skewed angle,  $\beta$ , distribution

boundary layer on the end wall, the flow which has a maximum  $\theta$  is regarded as the main flow, and the skew angle  $\beta$  is defined as  $\theta_{\max} - \theta$ . Then, the main flow component  $u$  and the secondary flow component  $w$  can be calculated with Eqs. (2) and (3).

The half-value breadth  $b$  obtained in the  $w$  distribution agreed with that obtained in  $U_r$  distribution within 3~4 per cent. The  $w/w_{\max}$ ,  $\tan \beta/\tan \beta_w$ , and  $u/U$  profiles against  $z/b$  also showed good agreement with the profiles in Fig. 12, 13 and 14, respectively. The three profiles at  $(r-R)/B = -0.5$  are indicated in Fig. 15(a)~(c) as circle marks, where the abscissa is not  $z/b$ , but  $z/l$  for  $l=2.5b$ .

It is observed in Fig. 15(a) that the main flow boundary layer thickness  $\delta_0$  is much thinner than the secondary flow boundary layer thickness  $l$ , whose flow situation can also be seen in the report by Senoo and Nishi<sup>(6)</sup>. Their measurements are indicated in Fig. 15 as triangle marks. Comparing the results of these two experimental measurements, the two profiles of  $u/U$  differ greatly from each other in Fig. 15(a), but in Fig. 15(b), the profile of  $\tan \beta/\tan \beta_w$ , both experimental results fall onto a line of  $(1 - z/l)^2$  given by Eq. (1).

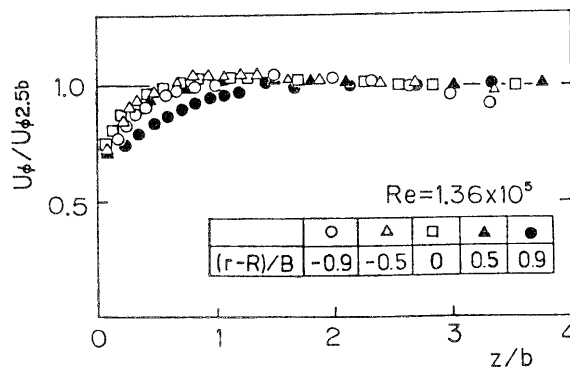
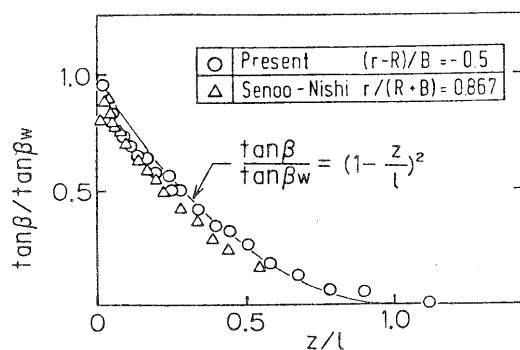


Fig. 14  $U_\phi/U_{\phi 2.5b}$  distribution

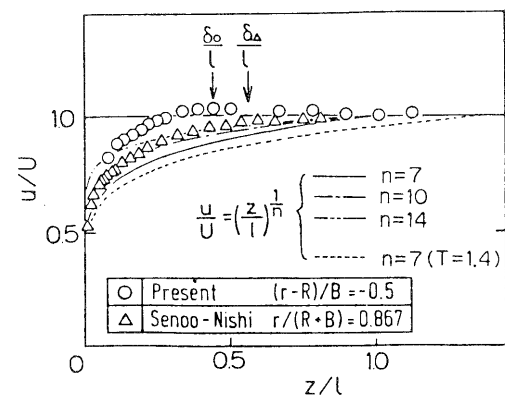


(b) Tangent of flow skewed angle,  $\tan \beta/\tan \beta_w$

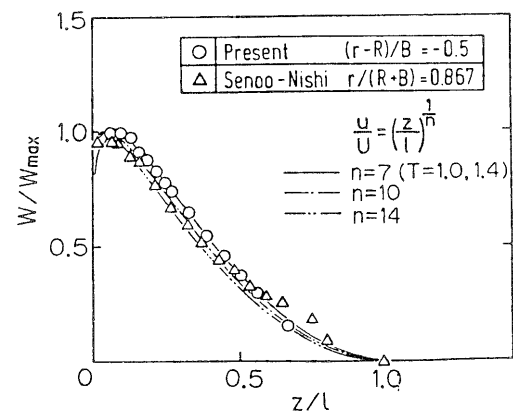
Nishi et al<sup>(9)</sup>, proposed to use and define two boundary layer thicknesses separately: one for the main flow and the other for the secondary flow. In the same paper, which treated a developing flow in a curved duct, they showed that the ratio of these two boundary layer thickness,  $T(=\delta/l)$ , varies linearly from 1.45 at the duct inlet ( $\phi=0^\circ$ ) to 0.65 at the  $\phi=60^\circ$  station, where  $\phi$  is the duct turning angle. The authors found that their measurements of  $\tan \beta/\tan \beta_w$  showed good agreement with Eq. (1), in spite of the changes in  $T$  in the developing flow region if the secondary flow boundary layer thickness  $l$  is used as a characteristic length.

Judging from the above - mentioned facts,  $\tan \beta/\tan \beta_w$  could be well represented by Eq. (1) for wide ranges of skewed boundary layers having any  $u/U$  profile and any value of  $T$ .

Figure 15(c) shows  $w/w_{\max}$  distributions, in which lines show the calculated profiles by Eq. (3), using Eq. (1) and four kinds of  $u/U$  profiles given in Fig. 15(a) by lines. The calculated  $w/w_{\max}$  depends on  $n$  and  $z/l$ , but not on  $T$ , as shown in the following:



(a) Main flow component,  $u/U$



(c) Secondary flow component,  $w/w_{\max}$

Fig. 15 Two boundary layer thicknesses:  $\delta$  for main flow and  $l$  for secondary flow

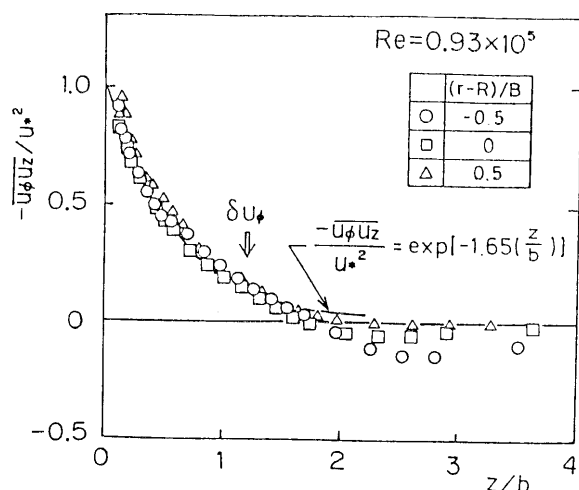


Fig. 16 Reynolds shear stress,  $-\rho \overline{u_\phi u_z}$

$$\frac{w}{w_{\max}} = \frac{(z/l)^{1/n} \cdot (1 - z/l)^2}{1/(2n+1)^{1/n} \cdot (1 - 1/(2n+1))^2} \quad (4)$$

Thus, the measured  $w/w_{\max}$  profile changes only slightly even for values of  $n$  from 7 to 14, and also agrees with both the measurements by Senoo et al. and by the present authors.

#### 5.4 Reynolds shear stress

Figure 16 shows the distributions of Reynolds shear stress  $-\rho \overline{u_\phi u_z}$  for  $z/b$  at  $(r-R)/B=0$ , and  $\pm 0.5$ . These results show quite well the existence of similarity and collapse onto a line given by

$$-\overline{u_\phi u_z} / u_*^2 = \exp(-1.65(z/b)).$$

$\delta u_\phi$  in the figure shows the main flow boundary layer thickness, where Reynolds shear stress  $-\rho \overline{u_\phi u_z}$  does not become zero, but still maintains 15 per cent of the wall shear stress. At  $z/b=1.8 \sim 2.0$ , the Reynolds shear stress becomes zero, and thereafter has a negative value, which might be due to the negative value of  $dU_\phi/dz$ .

#### 6. Conclusions

In this paper, turbulent flows in a curved duct of rectangular cross section having a small aspect ratio were studied experimentally. The data of the main flow were compared with those in ducts with large aspect ratios, and the following was concluded.

(1) A flow turning angle of more than a  $150^\circ$  is required for flow to reach a fully developed state in any duct having an aspect ratio  $H/B$  of its cross section ranging from 0.4 to 16. In the case of low aspect ratio, the main flow has a forced vortex-type velocity distribution, and has a free vortex-type distribution at a high aspect ratio.

(2) Concerning the boundary layers on the side walls, the ratio of  $\delta_{\log}$  to  $\delta$  ranges from 0.15 to 0.25. These values are not different from the ones obtained

for flat plate boundary layers.

(3) The Reynolds shear stress  $-\rho \overline{u_\phi u_z}$  becomes zero near  $z=\delta_{\log}$  in the inner wall boundary layer, but on the outer wall boundary layer, it becomes zero outside of the boundary layer.

Concerning the flow in the skewed boundary layer on the end plate,

(4)  $U_\phi$  profiles in the  $z$ -direction have a swelling near the end plate due to strong secondary flow, and are mostly similar and independent of their measured radial positions;

(5) secondary flow velocity profile is very similar to that of a two-dimensional wall jet, and the profile can hold for flows having almost any  $U_\phi$  profile;

(6) it might be convenient for fluid flow engineers to separately define two boundary layer thickness as Nishi et al.<sup>(9)</sup> did: one for the main flow and the other for the secondary flow;

(7) the secondary flow boundary layer thickness  $l$  can be defined as the distance from the wall which equals 2.5 times the half-value distance of the secondary flow velocity;

(8) with the characteristic length  $l$ , the profile of the flow skewing angle  $\beta$  from the main flow direction is represented by  $\tan \beta / \tan \beta_w = (1 - z/l)^2$  almost independently of the main flow velocity profiles;

(9) the profiles of Reynolds shear stress  $-\rho \overline{u_\phi u_z}$  have a common nondimensional profile when the secondary flow boundary layer thickness  $l$  is used as a characteristic length for the nondimensionalization. The magnitude of the shear stress decreases exponentially as one moves apart from the wall, but remains 15 per cent of the wall value, even at the main flow boundary layer edge.

#### Appendix

The maximum velocity was chosen as the characteristic velocity in the skewed boundary layer on the end wall, and represented by  $U$ . The distance from the wall at which  $U$  was obtained is denoted by  $\delta$ , at which point the direction of the flow is very close to that of the duct axis.

In the boundary layer, i. e.,  $0 < z < \delta$ , the function  $G$  in Eq. (2) is closely represented by  $(z/\delta)^{1/7}$ , and the function  $g$  in Eq. (3) by  $(1 - z/\delta)$  because  $\delta \ll l$ . Substituting these equations into Eq. (3), the calculated  $w$  value becomes a maximum at  $z/\delta = 1/8$ . The  $(rU_r)_{\min}$  value was estimated from  $u$  and  $w$  obtained at  $z/\delta = 1/8$ .

#### References

- (1) Senoo, Y., Energy Losses of Flow in Equilibrium Three-Dimensional Boundary Layer, Trans. J. Soc. Mech. Eng., (in Japanese), Vol. 47, No.



- 420(1975-8), p. 1459.
- (2) Wattendorf, F. L., A Study of the Effect of Curvature on Fully Developed Turbulent Flow, Proc. Royal Soc. of London, Vol. 148 (1934), p. 565.
  - (3) Eskinazi, S. and Yeh, H., An Investigation on Fully Developed Turbulent Flows in a Curved Channel, J. Aeronaut. Sci., Vol. 23 (1956-1), p. 23.
  - (4) Ellis, L. B. and Joubert, P. N., Turbulent Shear Flow in a Curved Duct, J. Fluid Mech., Vol. 62, Pt. 1 (1974), p. 65.
  - (5) Senoo, Y. and Nishi, M., Equilibrium Three-Dimensional Turbulent Boundary Layer on the End Wall of a Curved Channel, Proc. of 2nd Int. JSME Symp., (1972-9), p. 21.
  - (6) So, R. M. C. and Mellor, G. L., Experiment on Convex Curvature Effects in Turbulent Boundary Layers, J. Fluid Mech., Vol. 60, Pt. 1 (1973), p. 43.
  - (7) Gillis, J. C. and Johnston, J. P., Turbulent Boundary-Layer Flow and Structure on a Convex Wall and Its Redevelopment on a Flat Wall, J. Fluid Mech., Vol. 135 (1983), p. 123.
  - (8) Rajaratnam, N., Turbulent Jets, (in Japanese) (1981-7), p. 212, Morikita-Shuppan Co.
  - (9) Nishi, M., Senoo, Y., Ooho, T. and Sakamoto, H., Three-Dimensional Turbulent Boundary Layer on the End Plate of a Curved Duct, Prepr. of Jpn. Soc. Mech. Eng., (in Japanese), No. 730-16 (1973-10), p. 43.
-